Energy levels of few-electron quantum dots imaged and characterized by atomic force microscopy

Lynda Cockins[a], Yoichi Miyahara[a,1], Steven D. Bennett[a], Aashish A. Clerk[a], Sergei Studenikin[b], Philip Poole[b], Andrew Sachrajda[b], and Peter Grutter[a]

[a]Department of Physics, McGill University, 3600 rue University, Montreal, Quebec H3A 2T8, Canada; and [b]Institute for Microstructural Sciences, National Research Council of Canada, Ottawa, Ontario K1A 0R6, Canada

Edited by Robert Westervelt, Harvard University, Cambridge, MA, and accepted by the Editorial Board April 13, 2010 (received for review November 4, 2009)

Strong confinement of charges in few-electron systems such as in atoms, molecules, and quantum dots leads to a spectrum of discrete energy levels often shared by several degenerate states. Because the electronic structure is key to understanding their chemical properties, methods that probe these energy levels in situ are important. We show how electrostatic force detection using atomic force microscopy reveals the electronic structure of individual and coupled self-assembled quantum dots. An electron addition spectrum results from a change in cantilever resonance frequency and dissipation when an electron tunnels on/off a dot. The spectra show clear level degeneracies in isolated quantum dots, supported by the quantitative measurement of predicted temperature-dependent shifts of Coulomb blockade peaks. Scanning the surface shows that several quantum dots may reside on what topographically appears to be just one. Relative coupling strengths can be estimated from these images of grouped coupled dots.

nanoelectronics | single-electron charging | shell structure | electrostatic force microscopy

The ability to confine single charges at discrete energy levels makes semiconductor quantum dots (QDs) promising candidates as a platform for quantum computation (1, 2) and single-photon sources (3). Tremendous progress has been made not only in understanding the properties of single electrons in QDs but also in controlling their quantum states, which is an essential prerequisite for quantum computation (4). Single-electron transport measurements have been the main experimental technique for investigating electron tunneling into QDs (5). Charge sensing techniques using *built-in* charge sensors, such as quantum point contacts (6), complement transport measurements because lower electron tunneling rates can be monitored with even real-time detection being possible (7). It is instrumentally challenging to study self-assembled QDs via conventional transport and charge sensing methods because of the difficulty in attaching electrodes. Although progress is being made (8–12), these techniques have very small yield and therefore make it difficult to assess variation in QD electronic properties. Compared to typical QDs studied via transport measurements, in particular lithographically defined QDs, self-assembled QDs can be fabricated to have smaller sizes, stronger confinement potentials, and a more scalable fabrication process, all of which make them attractive for practical applications.

In this paper, we focus on an alternative technique for studying QDs that is better suited for self-assembled QDs: charge sensing by atomic force microscopy (AFM). Charge sensing by AFM is a convenient method to study the electronic structure of QDs because nanoelectrodes are not required and large numbers of QDs can be investigated in one experiment. Termed single-electron electrostatic force microscopy (*e*-EFM), this technique relies on the high force sensitivity of AFM to detect the electrostatic force resulting from single electrons tunneling into and out of the QD. It was first demonstrated on QDs formed in carbon nanotubes (13, 14) and later applied to self-assembled QDs (15, 16) and also to gold nanoparticles (17, 18). We focus on epitaxially grown self-assembled InAs/InP QDs in the few-electron regime. By using a dissipation model, we find compelling evidence for the existence of electronic degeneracies (i.e., shell structure) by measuring an effective temperature-dependent level repulsion of Coulomb blockade peaks in the AFM cantilever dissipation. This repulsion is a manifestation of the asymmetry between adding or removing electrons to or from a degenerate level on the dot; whereas similar effects were predicted for the conductance through a QD (19), we believe this to be a unique quantitative measurement. Further, we use the model to quantitatively extract various properties of both *individual* QDs, such as the tunneling rates and charging energy, and *coupled* QDs, such as the strength of coupling.

We study uncapped self-assembled InAs QDs grown on a 20-nm InP tunnel barrier, below which a two-dimensional electron gas (2DEG) is formed in an $In_{0.53}Ga_{0.47}As$ quantum well. A dc-bias voltage, V_B, is applied to the 2DEG with respect to the grounded conductive AFM cantilever tip. Fig. 1*A* shows the sample structure and experimental setup. The AFM cantilever is driven at its mechanical resonance frequency, $\omega_0/2\pi \sim 166$ kHz, with constant oscillation amplitude (20). The voltage drop, αV_B ($\alpha < 1$), across the tunnel barrier between the QD and the 2DEG is only a fraction of V_B, with $\alpha = \alpha(x,y,z)$ being a function of the tip position. The tip–QD gap is tens of nanometers wide so that tip–QD tunneling is negligible. We thus have a single-electron box setup: The electrochemical potential of the 2DEG, μ_{2DEG}, with respect to the QD, μ_{QD}, is set by αV_B and a negative bias increases the number of electrons, N, on the QD in integer steps whenever the electrochemical potentials are aligned (called a charge degeneracy point). Tunneling between 2DEG and QD is suppressed by the electrostatic energy cost, E_C, of adding or removing an electron to the QD except near these charge degeneracy points (Coulomb blockade). The heart of the *e*-EFM technique lies in the fact that oscillations of the AFM cantilever modulate α and hence are equivalent to an effective oscillating gate voltage applied to the QD. Thus, motion of the cantilever induces a modulation of N that will be slightly out of phase with the cantilever's motion (a result of the finite response time of electrons on the dot). The electrostatic coupling between QD and cantilever tip implies an electrostatic force proportional to N acting on the tip, the net result being both a frequency shift, $\Delta\omega$, and additional dissipation, γ, of the cantilever (21). These effects are maximal at charge degeneracy points because here N can easily change in response to the effective oscillating gate voltage.

Author contributions: Y.M. and P.G. designed research; L.C., Y.M., S.D.B., and A.A.C. performed research; S.S. and P.P. contributed new reagents/analytic tools; L.C., Y.M., S.D.B., and A.A.C. analyzed data; and L.C., Y.M., S.D.B., A.A.C., S.S., P.P., A.S., and P.G. wrote the paper.

The authors declare no conflict of interest.

This article is a PNAS Direct Submission. R.W. is a guest editor invited by the Editorial Board.

[1]To whom correspondence should be addressed. E-mail: miyahara@physics.mcgill.ca.

This article contains supporting information online at www.pnas.org/lookup/suppl/doi:10.1073/pnas.0912716107/-/DCSupplemental.

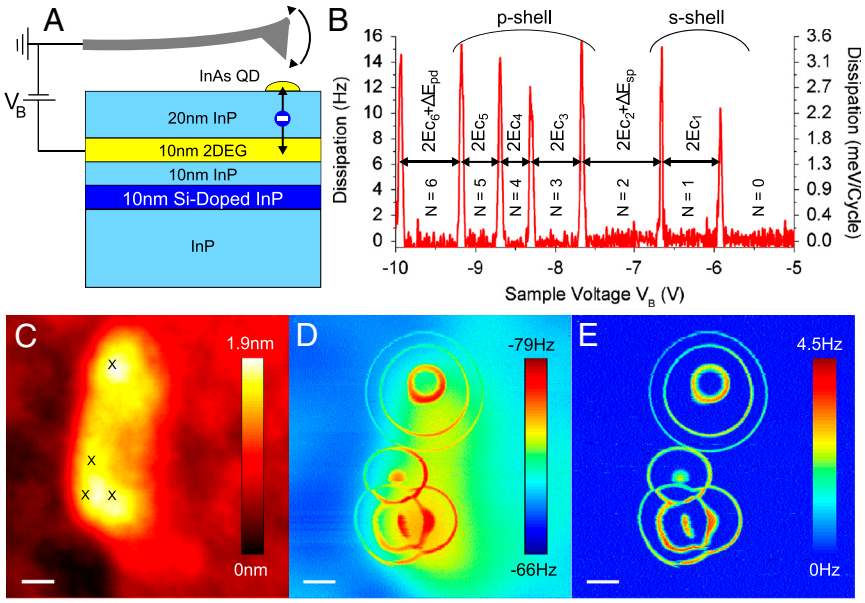

Fig. 1. *e*-EFM V_B spectra and images. (*A*) Schematic of the oscillating cantilever with pyramidal tip pushing electrons on and off the QD when the mean bias voltage is just enough to lift the Coulomb blockade. (*B*) γ-V_B spectra taken at 4.5 K over upper QD shown in *E*. Peaks in the spectra are always separated by the charging energy, but shells are additionally separated by ΔE. After passing each peak from right to left, the number of electrons, *N*, in the QD increases by one, with the $N = 7$ state after the leftmost peak. The energy difference between the first two peaks is 31 meV, and the difference between peaks 2 and 3 is 42 meV, so that if $2E_C$ between peaks 2 and 3 is assumed to be 31 meV, then $\Delta E_{sp} = 11$ meV. (*C*) Topography of the InAs island with the approximate locations of the QDs marked by Xs. (*D* and *E*) The simultaneously recorded frequency shift and dissipation images of the structure in *C* at 4.5 K taken at −8 V. (Scale bar: 20 nm.)

Fig. 1*B* is an example of $\gamma(V_B)$ at 4.5 K with the tip positioned over the upper QD imaged in Fig. 1 *D*–*E*. The $\gamma(V_B)$ is equivalent to the energy addition spectra usually obtained from linear conductance or capacitance spectroscopy measurements (22). Similar to those measurements, Coulomb blockade peaks in γ occur near charge degeneracy points of the QD. The peak positions are suggestive of the addition spectrum of a 2D circular QD with a parabolic confinement potential; each peak is separated by twice the capacitive charging energy, $2E_C$, with a further splitting between peaks 2 and 3 and between peaks 6 and 7 corresponding to the energy difference between shells, ΔE. This type of shell structure has been previously observed in InAs QDs (8, 9, 23, 24). Fig. 1 *C*–*E* shows the topography, $\Delta\omega$, and γ images of an elongated InAs island. The peaks in the γ-V_B spectra radially surround the QD center so that the ring furthest from the center corresponds to the first electron entering the QD; the rings themselves are contour lines of constant αV_B. Multiple sets of concentric rings appearing in the $\Delta\omega$ and γ images indicate multiple QDs in the island. Such observations would not be as easily identified via other experimental means (25). The tip–2DEG capacitive force adds a large background in the $\Delta\omega$ signal that locally varies because of topography (15, 26), making it advantageous to focus on the γ for image analysis.

Fig. 2*A* shows γ and $\Delta\omega$ as a function of V_B with the tip positioned over the upper QD imaged in Fig. 1 *D*–*E* at 30 K. Whereas the energy addition spectra shown in Figs. 1*B* and 2*A* are consistent with the expected shell structure for a 2D circular QD with a parabolic confinement potential, we obtain much stronger evidence of the shell structure from the temperature dependence of the peak positions. Theoretically, temperature-dependent shifts of Coulomb blockade peaks are expected whenever one has degenerate single particle levels, as predicted for the conductance peaks of a spin degenerate level (19). These shifts are a consequence of the asymmetry between adding or removing electrons; the direction of each peak shift versus V_B depends on whether there are more ways to add or to remove an electron. These asymmetries for a twofold degenerate *s* shell and a fourfold degenerate *p* shell (expected for a circular QD) are illustrated in Fig. 3. The size of each shift is proportional to temperature, which enters through the Fermi distribution of electrons in the 2DEG, with a numerical prefactor that depends on how asymmetric the addition and removal processes are. The result is an effective temperature-dependent energy level repulsion: The peaks in each shell move apart as temperature is increased. Furthermore, our theoretical analysis (*SI Text*) suggests that this effect should be enhanced in the tunneling-induced cantilever dissipation compared to the conductance. Our measurements of these temperature-dependent peak shifts are in excellent agreement with theory; we are unaware of any experiments where these effects have been observed.

We model the dissipation on the cantilever by using linear response and a master equation describing the charge state of the QD in the regime of weak coupling (19, 27). Details of the approach are provided in *SI Text*. Near a charge degeneracy point between N and $N + 1$ electrons on the QD where the extra electron occupies a nondegenerate single particle level, the dissipation is (18, 28)

$$\gamma = \frac{\omega_0^2 A^2 \Gamma}{k_0 k_B T} \frac{1}{\omega^2 + \Gamma^2} f(1-f), \qquad [1]$$

where ω_0 and k_0 are the intrinsic cantilever resonance frequency and spring constant, respectively, $\omega = \omega_0 + \Delta\omega$ is the measured resonance frequency because of forces on the cantilever, and $f = 1/(1 + \exp(E/k_B T))$ is the Fermi function evaluated at $E = \mu_{QD} - \mu_{2DEG} = e\alpha(V_B + V_0)$ ($V_B = -V_0$ is the point of charge degeneracy). The temperature, Boltzmann constant, and electron charge are described by T, k_B, and e, respectively. In the nondegenerate case, the rate to add an electron to the QD is $\Gamma_+ = \Gamma f$ and the rate to remove an electron is $\Gamma_- = \Gamma(1-f)$, where Γ is the 2DEG–QD tunneling rate. Last, $A = -2E_C \frac{V_B}{e}(1-\alpha)\frac{\partial C_{tip}}{\partial z}$ is the sensitivity of the potential on the QD to the cantilever motion and C_{tip} is the tip–QD capacitance. We stress that Eq. **1** applies to each dissipation peak independently: Γ and A are obtained separately for each peak from the data with no assumption of constant E_C.

Whereas it describes the broadening of each peak very well, Eq. **1** only takes into account a single nondegenerate level. More generally, suppose the QD is occupied by $N + 1$ electrons, with $n_{shell} + 1$ in the valence shell. If this shell is ν-fold degenerate, then near the charge degeneracy point between N and $N + 1$ electrons on the QD, the dissipation is

$$\gamma(V_B) = \frac{\omega_0^2 A^2 \Gamma}{k_0 k_B T} \frac{(n_{shell}+1)(\nu - n_{shell})}{\omega^2 + (\phi\Gamma)^2} \frac{f(1-f)}{\phi}, \qquad [2]$$

where

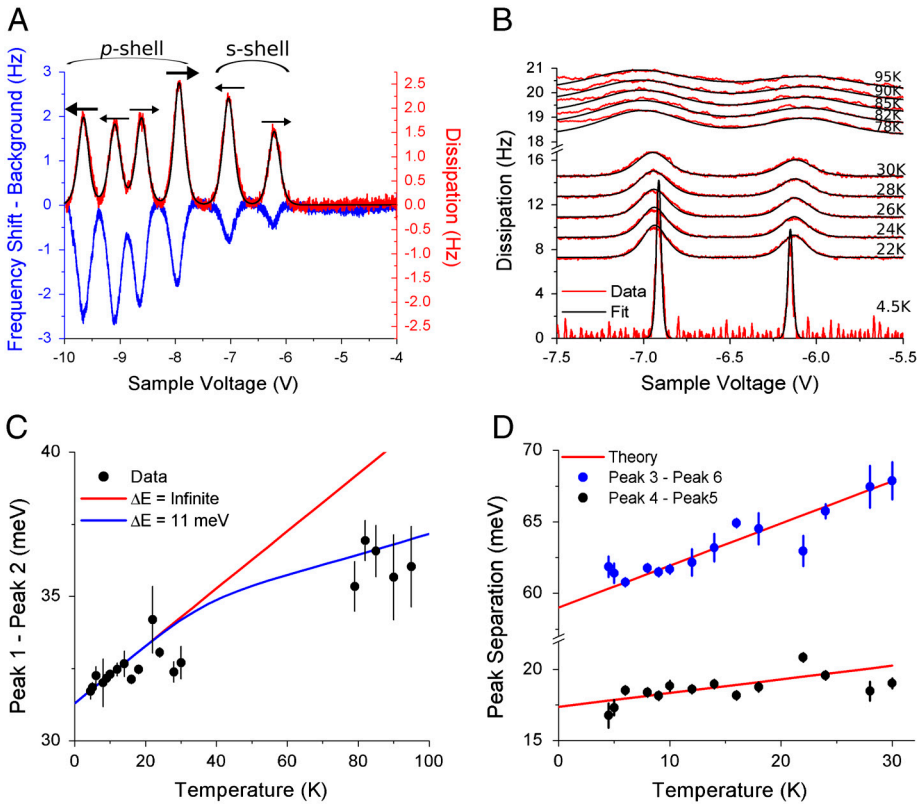

Fig. 2. Temperature-dependent shifts of Coulomb blockade peaks. (*A*) The dissipation γ (*Red*) and frequency shift $\Delta\omega_{dip}$ (*Blue*) measured simultaneously versus bias voltage, V_B, over the center of the upper set of concentric rings in Fig. 1*E*. Note that the parabolic background from the capacitive force has been subtracted from $\Delta\omega$ to show $\Delta\omega_{dip}$ (see *Materials and Methods*). The lever arm, α, is determined by fitting each peak to Eq. **2** (*Black*). (*B*) The first two peaks from the right in γ fitted to Eq. **2** at different temperatures (offset for clarity). (*C*) The measured and theoretical separation between peaks 1 and 2 as a function of temperature where the sole fit parameter is the peak separation at zero temperature, $2E_{C1} = 31$ meV. A numerical calculation of this separation including the effects of the empty *p* shell is also shown (*Blue*). (*D*) The separation between peaks 3 and 6 and peaks 4 and 5. Because of thermal broadening of the peaks, the positions of these peaks could be determined only up to 30 K. The directions and magnitudes of the peak shifts as a function of temperature are indicated with arrows in *A* with larger arrows indicating greater shifts.

$$\phi = (\nu - n_{shell})f + (n_{shell} + 1)(1 - f), \quad [3]$$

and Γ is the tunneling rate to one particular state on the QD, assumed to be equal for each degenerate state within the ν-fold degenerate shell.* Note that n_{shell} is the number of electrons occupying the given shell and not the total number of electrons on the dot, N. Because of the factor ϕ, $\gamma(V_B)$ is no longer symmetric about its maximum, and the different coefficients of f and $1 - f$ in ϕ reflect that the rates to add and remove electrons are now asymmetric: $\Gamma_+ = (\nu - n_{shell})\Gamma f$ and $\Gamma_- = (n_{shell} + 1)\Gamma(1 - f)$. Note that a nondegenerate level corresponds to $\nu - n_{shell} = n_{shell} + 1 = 1$, for which Eq. **2** reduces to Eq. **1**. The asymmetry in Eq. **2** causes each peak in $\gamma(V_B)$ to be shifted by an amount proportional to temperature, because a dissipation peak maximum roughly corresponds to maximal tunneling on and off the dot, and this is achieved when the addition and removal rates are equal.† The connection between the peak shifts and asymmetric addition and removal rates is depicted schematically in Fig. 3. By fitting $\gamma(V_B)$ (e.g., Fig. 2*A*) to Eq. **2**, we extract α, allowing us to convert the V_B axis into energy. This is done for all of the thermally limited peaks, yielding $\alpha = 0.036 \pm 0.003$. Fig. 2*B* shows $\gamma(V_B)$ at different temperatures together with the fitted curves.

The role of ϕ is further elucidated by the relation

$$\phi\Gamma = -2\omega_0 \frac{\Delta\omega_{dip}}{\gamma}, \quad [4]$$

where $\Delta\omega_{dip}$ is the size of the frequency shift dip because of the single-electron tunneling. The ratio in Eq. **4** defines an inverse time scale set by the relative in-phase and out-of-phase parts of the electrostatic force; this is simply Γ for a nondegenerate QD (18, 28) but modified by degeneracy through the factor ϕ. By using Eqs. **2** and **4** and the measured values of γ and $\Delta\omega_{dip}$, we calculate the tunneling rates at the maxima of dissipation peaks 1–6, obtaining $\Gamma/2\pi = 70$, 90, 160, 180, 230, and 330 kHz. As expected, Γ increases with increasing V_B as the height of the potential barrier between the 2DEG and the QD is reduced.

After extracting the tunneling rates, we fit each dissipation peak by using Eq. **2** and measure the spacing between peaks as functions of temperature from 4.5 to 30 K and from 78 to 95 K. We focus on the relative shifts between peaks, because these are less sensitive than the absolute peak positions to slight offsets because of small changes in the tip–QD distance. The size and direction of each peak shift is different (see Fig. 2*A*), in a manner that is completely captured by our model: The two peaks in the *s* shell shift apart, as do the four peaks in the *p* shell. The measured relative peak shifts of repelling pairs are shown in Fig. 2 *C–D* and compared to the theoretical shifts from Eq. **2**, where the sole fit parameter is the *y* intercept corresponding to $2E_C$. In addition, we expect that multiple shells, not just the valence shell, should play a role at high temperatures where $k_BT \ll \Delta E$ is not satisfied. For the relative shift of peaks 1 and 2 (Fig. 2*C*) we plot a numerical calculation accounting for the possible occupation of the *p* shell, showing that the high temperature correction agrees well with the data. Fig. 2*D* shows that the relative shifts between peaks 3 and 6 and between 4 and 5 are well described by Eq. **2** up to 30 K. Finally, we note that there is an overall shift of the *s* and *p* shells toward each other that we believe is a consequence of strong repulsion of the *p* shell by the *d* shell, predicted to be sixfold degenerate.

The agreement between the data and theory shown in Fig. 2 *C–D* is strong evidence that the peak shifts are because of level degeneracy in the QD. We performed several additional checks to support this conclusion. First, our explanation of the observed peak shifts requires only approximate level degeneracies, and the predicted shifts are unchanged provided that the degeneracy splitting is smaller in energy than k_BT. This is important because

*We checked that taking distinct rates for each degenerate state leads to no qualitative change in the results (see *SI Text*).

†The correspondence between dissipation peak positions and maximal tunneling is only approximate because of an extra dependence on ϕ (see *SI Text*).

we expect level degeneracies to be lifted in the real, imperfect QDs that we measure. We note that, according to our theory, the observation of peak shifts down to 4.5 K implies that the level splitting is smaller than this temperature corresponding to roughly 0.4 meV. Furthermore, the same degeneracy theory leads to small, but measurable, shifts between the dissipation peak and the frequency peak corresponding to the same charge degeneracy point. This is visible for the third peak (from the right) in Fig. 2*A* in which the γ and $\Delta\omega$ peaks do not exactly line up, with the measured shifts compared to theory in Fig. S1 (see *SI Text*). These dissipation-frequency shifts further support our model, ruling out the alternative of a temperature-dependent renormalization of E_C or ΔE.

Finally, before we discuss results for coupled QDs, it is worth noting that our theoretical treatment of degeneracies also predicts that the Coulomb blockade cantilever dissipation peaks should have a slightly asymmetric line shape; cf. Eq. **2**. This effect was unfortunately too small to be resolved in the current experiment, which focuses on cantilever–dot couplings that are weak enough that the motion of the cantilever only weakly perturbs the dot. We recently studied both theoretically and experimentally the more complex regime where this coupling strength becomes strong, because of a much larger cantilever oscillation amplitude. We find that in this strong coupling regime, degeneracy-induced line shape asymmetries become much more pronounced and clearly resolvable (29).

Significant efforts are ongoing towards understanding and controlling the properties of coupled QDs, in particular double QDs or "artificial molecules" (30). The γ images that we obtain for double QDs are equivalent to stability diagrams that depict the charge state of the double QD system. This is because of the position dependence of the lever arm $\alpha(x,y,z)$ for each QD that results in two electrochemical potentials, μ_{QD1} and μ_{QD2}. Scanning the AFM tip at constant height and V_B corresponds to sweeping the μ_{QD1}–μ_{QD2} space through changing α_1 and α_2 even though only a single electrode (the tip) is being used. In a conventional stability diagram, lines of constant electrochemical potential for each QD are plotted as a function of two gate voltages. When the two QDs are coupled, intersection points are split into two points (triple points), showing avoided crossings (30). In the γ images the avoided crossings are observed when the ring radii suddenly change at intersection points. Fig. 4 *A* and *B* show the same three QDs as in the lower part of Fig. 1*E*, now imaged at −9 and −7.6 V, respectively. Such avoided crossings are highlighted in the circle and box in Fig. 4*A*, representing an example of weak and strong coupling, respectively.

We characterize the coupling strength by comparing the ratio of the change in ring radius to the separation between the first two rings ($2E_C$) for QD2 (30). This method is valid only when both rings are far enough from the QD center that the voltage drop between them is approximately linear. By following this procedure, the coupling of QD2 to QD1 (circle) and QD3 (box) can be compared. Whereas the change in radius of QD2 is approximately 0.10 ± 0.01 of $2E_C$ because of QD1, it is 0.46 ± 0.03 because of QD3, indicating a much stronger coupling between QD2 and QD3. We consider the former to be an example of weak coupling because the triple points are nearly joined. This is consistent with a small capacitive coupling between the two dots: The charging of one dot effectively gates the second dot, causing a sudden change in ring radius.

Conversely, the boxed region in Fig. 4*A* is an example of strong coupling because there is a large gap at ring intersections as in the triple points of a stability diagram. In Fig. 4*B*, the same three QDs as in Fig. 4*A* are imaged at smaller V_B. This image allows for a more intuitive explanation of the coupling. Consider the diagonal line from the center of QD3 outward; initially, the AFM tip is over QD3 in the $(N_{QD2},N_{QD3}) = (0,1)$ state but takes a path into QD2 in the $(1,0)$ state. The ability to go continuously between these states without going through $(0,0)$ or $(1,1)$ necessarily indicates a large capacitive coupling between the dots. It also indicates evidence for an interesting charge transfer process because no dissipation is observed between circles. Lack of dissipation implies no change in the total dot charge; either there is a cotunneling process where two electrons simultaneously tunnel to and from the 2DEG, or there is coherent tunneling between the dots.

Fig. 4 *C–E* shows another example of coupled QDs at 4.5 K. The InAs structure (Fig. 4*C*) contains coupled QDs as shown in the γ image (Fig. 4*D*). Fig. 4*E* zooms up on the region in Fig. 4*D* showing many avoided crossings. Within this distance range from the QD centers, each α is approximately linearly dependent on the tip position so that scanning the tip more closely resembles sweeping two gate voltages, resulting in the image resembling a conventional stability diagram. Fig. 4 also highlights how advantageous it is to have images in addition to the γ-V_B spectra be-

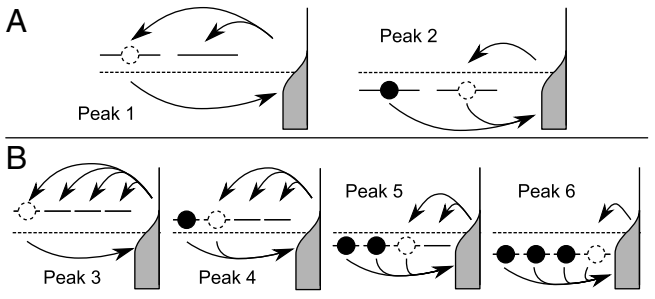

Fig. 3. The asymmetry between adding and removing electrons because of degeneracy on the QD. Solid horizontal lines depict electronic states on the QD, and the Fermi distribution of electrons in the 2DEG is shown in gray. Solid circles represent electrons already on the QD, whereas an empty dashed circle is a newly added electron. The fine dashed line is where the chemical potentials line up and where a dissipation peak occurs for a nondegenerate level. The levels must be shifted as shown to recover equal addition and removal rates. (*A*) Addition and removal processes in the *s* shell of degeneracy $\nu = 2$. For the first peak the QD is initially empty ($n_{shell} = 0$), so there are two possible states to tunnel into, but only one way to remove an electron once it has tunneled in. For the second peak the shell is already occupied by one electron ($n_{shell} = 1$), so there is only one way to tunnel in but either electron may be removed. (*B*) Addition and removal processes in the *p* shell of degeneracy $\nu = 4$. Peaks 3–6 correspond to initial *p* shell filling of $n_{shell} = 0$–3.

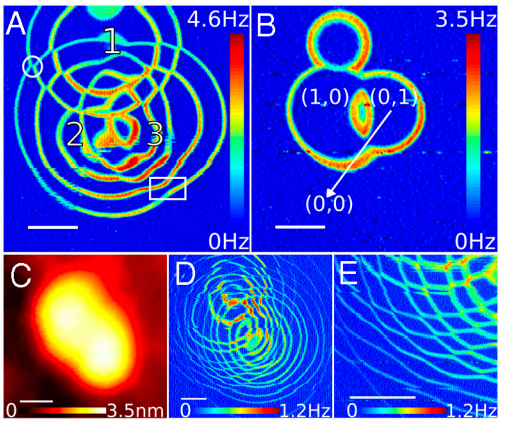

Fig. 4. Imaging coupled QDs. (*A*) Dissipation image showing the same three QDs as the lower half of Fig. 1*E* taken at a larger bias voltage, $V_B = -9$ V. (*B*) Dissipation image of the same region as *A* taken at $V_B = -7.6$ V. The three QDs are numbered in *A* but are easier to identify in *B* because each QD contains one electron. In *A* an example of weak coupling between QD1 and QD2 is circled, and an example of strong coupling between QD2 and QD3 is boxed. The possible mechanisms are discussed in the text. (*C*) Topography of two connected islands. (*D*) Dissipation image taken at $V_B = -8.0$ V of the structure in *C*. Each structure in *C* appears to have an associated QD. (*E*) Dissipation image of region in *D* with many anticrossings. (Scale bar: 20 nm.)

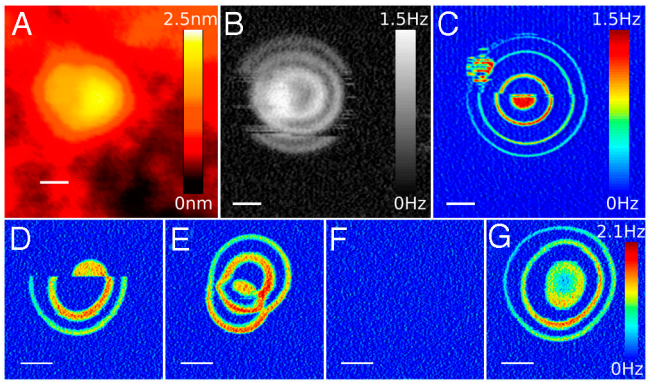

Fig. 5. Imaging charge noise. (*A*) Topography of QD. (*B*) Dissipation image of *A* at 78 K. Middle sections of the outermost ring are missing, which indicates reconfiguration of nearby charge. (*C*) Dissipation image of *A* at 4.5 K. The slight discontinuity between the upper and lower half of the rings indicates that the energy levels of the QD shifted toward μ_{2DEG} in the lower half. Perhaps the cause of the "charge noise" is the emerging QD in the upper left corner of *C* that is in the vicinity of a small protrusion of the structure in *A*. (*D*) Dissipation image of a different QD at 4.5 K with $V_B = -8.0$ V. During one horizontal scan line (slow scan direction is upward), the confinement potential abruptly changes. (*E*) Dissipation image of the same region as *F* at $V_B = -9.0$ V where coupled QDs are now present. (*F*) Dissipation image taken at $V_B = +6.8$ V revealing no features as the QD is empty. (*G*) Dissipation image taken immediately after *F* at $V_B = -8.0$ V. The original confinement potential was restored. (Scale bar: 20 nm.) *D*–*G* share the same color bar.

cause the spectra alone will contain the peaks from nearby QDs that can be identified by using the images.

Yet another advantage of this technique is the ability to spatially resolve the effects of changes in the local electrostatic environment; for self-assembled QDs, no other technique is capable of doing this. The AFM images show how the QD confinement potential is being influenced by charge reconfiguration. Fig. 5 shows two such cases. The structure in Fig. 5*A* shows a fluctuation in electron population because of nearby fluctuations in the electrostatic background at both 78 (Fig. 5*B*) and 4.5 K (Fig. 5*C*). The missing sections of the first ring in Fig. 5*B* indicate that the number of electrons in the QD is fluctuating by one in this region. Interestingly, depending on the scan direction (left to right or right to left) over the QD, the missing section may appear. A similar reconfiguration was observed in the γ-V_B spectra. Whereas all the peaks appear in the reverse V_B sweep (positive to negative), the first peak disappears in the forward sweep. Fig. 5 *D*–*G* shows a more dramatic change. During the scan, a sudden switch in the confinement potential occurs, leading to the transition from the single QD (Fig. 5*D*) to a coupled double QD (Fig. 5*E*). This double QD state could be switched back to the single state (Fig. 5*G*) by scanning over the same area with a positive V_B (Fig. 5*F*). Although both of these changes are readily identified in the images, having a spectrum alone may cause confusion as is the case in conventional transport measurements. These observations indicate that the QD confinement potentials are very sensitive to the electrostatic background and can be modified, or switched, controllably.

Charge sensing with AFM can be used to investigate the electronic structure of single and coupled self-assembled QDs. The technique enables the quantitative extraction of the tunneling rate, charging energy, and the QD interaction energies; further, we have used it to perform a unique measurement of temperature-dependent Coulomb blockade peak shifts confirming the shell degeneracy of the QD. The dissipation images proved especially useful in analyzing multiple QDs and changes in QD confinement potential resulting from nearby charge fluctuations. The images also revealed that what looked like a single QD structure topographically can actually contain multiple QDs, which might be a result of the local modulation of the confinement potential caused by oxidation or structural defects. Additionally, the imaging capability of AFM provides insight into the link between QD electronic structure and topography, which is of great importance in developing electronic devices on the basis of QDs.

Materials and Methods

Sample. The sample, grown by chemical beam epitaxy (31), consists of the following layers: 460 nm undoped InP grown on top of an insulating InP substrate, followed by a 10 nm Si-doped InP layer, 10 nm undoped layer, 10 nm $In_{0.53}Ga_{0.47}As$ layer, 20 nm undoped layer, and a 1.82 ML InAs layer that results in the formation of InAs QDs by Stranski–Krastanow growth. The QDs cover the surface with a density of ~2.5 QDs per μm^2 having diameters in the range of 30–95 nm and heights of 0.5–6 nm. The 2DEG layer formed in the InGaAs well serves as a back electrode, and an Ohmic contact to the 2DEG is made by indium diffusion.

Experiment and Data Processing. Our home-built cryogenic AFM (32) includes an rf-modulated fiber optic interferometer (33) with 1,550-nm wavelength for cantilever position detection. We coat Si AFM cantilevers (Nanosensors PPP-NCLR) with 10 nm titanium (adhesion layer) and 20 nm platinum. The cantilevers typically have a spring constant of $k \approx 48$ N/m, with a 160 kHz resonance frequency and a quality factor, Q, between 100,000 and 200,000 at 4.5 K. All of the images were taken in frequency modulation mode (20). In this mode, the cantilever is self-oscillated at its resonance frequency with a constant amplitude. The frequency shift and dissipation were measured with a commercially available phase-locked loop frequency detector (Nanosurf, easyPLL plus). The topography images were taken in constant frequency shift mode where a constant frequency shift is maintained by regulating the cantilever tip–sample distance by using a feedback controller. The frequency shift and dissipation images were taken in constant-height mode with a typical tip height of 20 nm. Dissipation images are shown in Fig. S2 as a function of V_B. More negative V_B results in adding more electrons to the QD. Areas of increased dissipation mark 2DEG–QD tunneling events. Each time a ring is crossed when traveling toward the quantum dot center marks the addition of an electron to the dot. More details of the AFM images are listed in Table S1. The amplitude of the cantilever excitation signal, A_{exc}, is provided as the dissipation signal from the Nanosurf oscillator controller. It is converted to units of 1/s via $\frac{\omega_0}{Q}\left(\frac{A_{exc}}{A_{exc0}} - 1\right)$. A_{exc0} is the excitation amplitude independent of the tunneling process, in other words, the background dissipation. This conversion is independent of cantilever oscillation amplitude. Similarly, the signal is converted to units of eV/cycle by multiplying $\frac{A_{exc}}{A_{exc0}} - 1$ by the factor $E_0 = \frac{\pi k_0 a^2}{eQ}$, where a is the cantilever oscillation amplitude (34). The $\Delta\omega - V_B$ spectra shown in Fig. 2*A* was originally superposed onto a large parabolic background arising from the capacitive force between the 2DEG and cantilever tip. Over several volts, at typical cantilever–sample gaps of 20 nm, the curve can be fit with a single parabola. In Fig. 2*A* this parabola was subtracted from the frequency shift data.

The exact positions of the peaks (dips) in the dissipation (frequency shift) are sensitive to the distance between cantilever tip and QD. In particular, slight changes in cantilever tip lateral position with respect to the QD center can lead to slight shifts in the peaks as can be deduced from the images where the rings can have different spacing depending on location. The shift in peaks as a function of height, however, is linearly dependent over the distances used in this experiment (12–22 nm). We took the differences in peak positions in the data displayed in Fig. 2*B* to be caused by small height differences (sub-1 nm), and so the voltage axis was rescaled to align the data peaks with the theoretical peaks but the peak heights were not rescaled. The mean factor involved in the voltage rescaling is 1.011 with the most extreme factor being 1.088. The temperature data above 22 K had thermally limited peaks for a cantilever oscillation amplitude of 0.4 nm but needed to be reduced to 0.2 nm at 4.5 K. The error bars in Fig. 2 *C* and *D* represent how well the measurement over a single location was reproduced.

ACKNOWLEDGMENTS. Funding for this research was provided by the Natural Sciences and Engineering Research Council of Canada, le Fonds Québécois de le Recherche sur la Nature et les Technologies, the Carl Reinhardt Fellowship, and the Canadian Institute for Advanced Research.

1. Loss D, DiVincenzo DP (1998) Quantum computation with quantum dots. *Phys Rev A* 57:120–126.

2. Tanamoto T (2000) Quantum gates by coupled asymmetric quantum dots and controlled-not-gate operation. *Phys Rev A* 61:022305.

3. Dalacu D, et al. (2010) Directed self-assembly of single quantum dots for telecommunication wavelength optical devices. *Laser Photonics Rev* 4:283–299.
4. Hanson R, Kouwenhoven LP, Petta JR, Tarucha S, Vandersypen LMK (2007) Spins in few-electron quantum dots. *Rev Mod Phys* 79:1217–1265.
5. Kouwenhoven LP, Austing DG, Tarucha S (2001) Few-electron quantum dots. *Rep Prog Phys* 64:701–736.
6. Field M, et al. (1993) Measurements of Coulomb blockade with a noninvasive voltage probe. *Phys Rev Lett* 70:1311–1314.
7. Lu W, Ji Z, Pfeiffer L, West KW, Rimberg AJ (2003) Real-time detection of electron tunnelling in a quantum dot. *Nature* 423:422–425.
8. Ota T, et al. (2004) Single-dot spectroscopy via elastic single-electron tunneling through a pair of coupled quantum dots. *Phys Rev Lett* 93:066801.
9. Jung M, et al. (2005) Shell structures in self-assembled InAs quantum dots probed by lateral electron tunneling structures. *Appl Phys Lett* 87:203109.
10. Igarashi Y, et al. (2007) Spin-half Kondo effect in a single self-assembled InAs quantum dot with and without an applied magnetic field. *Phys Rev B* 76:081303.
11. Vdovin EE, et al. (2007) One-electron spin-dependent transport in split-gate structures containing self-organized InAs quantum dots. *J Exp Theor Phys* 105:145–148.
12. Amaha S, et al. (2008) Laterally coupled self-assembled InAs quantum dots embedded in resonant tunnel diode with multigate electrodes. *Appl Phys Lett* 92:202109.
13. Woodside MT, McEuen PL (2002) Scanned probe imaging of single-electron charge states in nanotube quantum dots. *Science* 296:1098–1101.
14. Zhu J, Brink M, McEuen PL (2005) Frequency shift imaging of quantum dots with single-electron resolution. *Appl Phys Lett* 87:242102.
15. Stomp R, et al. (2005) Detection of single-electron charging in an individual InAs quantum dot by noncontact atomic-force microscopy. *Phys Rev Lett* 94:056802.
16. Dana A, Yamamoto Y (2005) Electrostatic force spectroscopy of near surface localized states. *Nanotechnology* 16:S125–S133.
17. Azuma Y, Kanehara M, Teranishi T, Majima Y (2006) Single electron on a nanodot in a double-barrier tunneling structure observed by noncontact atomic-force spectroscopy. *Phys Rev Lett* 96:016108.
18. Zhu J, Brink M, McEuen PL (2008) Single-electron force readout of nanoparticle electrometers attached to carbon nanotubes. *Nano Lett* 8:2399–2404.
19. Beenakker CWJ (1991) Theory of Coulomb-blockade oscillations in the conductance of a quantum dot. *Phys Rev B* 44:1646–1656.
20. Albrecht TR, Grütter P, Horne D, Rugar D (1991) Frequency modulation detection using high-q cantilevers for enhanced force microscope sensitivity. *J Appl Phys* 69:668–673.
21. Hölscher H, et al. (2001) Measurement of conservative and dissipative tip-sample interaction forces with a dynamic force microscope using the frequency modulation technique. *Phys Rev B* 64:075402.
22. Ashoori RC, et al. (1992) Single-electron capacitance spectroscopy of discrete quantum levels. *Phys Rev Lett* 68:3088–3091.
23. Drexler H, Leonard D, Hansen W, Kotthaus JP, Petroff PM (1994) Spectroscopy of quantum levels in charge-tunable InGaAs quantum dots. *Phys Rev Lett* 73:2252–2255.
24. Miller BT, et al. (1997) Few-electron ground states of charge-tunable self-assembled quantum dots. *Phys Rev B* 56:6764–6769.
25. Zhitenev NB, Brodsky M, Ashoori RC, Pfeiffer LN, West KW (1999) Localization-delocalization transition in quantum dots. *Science* 285:715–718.
26. Cockins L, Miyahara Y, Stomp R, Grutter P (2007) High-aspect ratio metal tips attached to atomic force microscopy cantilevers with controlled angle, length, and radius for electrostatic force microscopy. *Rev Sci Instrum* 78:113706.
27. Clerk AA, Bennett S (2005) Quantum nanoelectromechanics with electrons, quasiparticles and cooper pairs: effective bath descriptions and strong feedback effects. *New J Phys* 7:238.
28. Brink M (2007) Imaging single-electron charging in nanostructures by low-temperature scanning force microscopy. Ph.D. thesis (Cornell University, Ithaca, NY).
29. Bennett SD, Cockins L, Miyahara Y, Grütter P, Clerk AA (2010) Strong electromechanical coupling of an atomic force microscope cantilever to a quantum dot. *Phys Rev Lett* 104:017203.
30. van der Wiel WG, et al. (2002) Electron transport through double quantum dots. *Rev Mod Phys* 75:1–22.
31. Poole PL, McCaffrey J, Williams RL, Lefebvre J, Chitrani D (2001) Chemical beam epitaxy growth of self-assembled InAs/InP quantum dots. *J Vac Sci Technol B* 19:1467–1470.
32. Roseman M, Grutter P (2000) Cryogenic magnetic force microscope. *Rev Sci Instrum* 71:3782–3787.
33. Rugar D, Mamin HJ, Guethner P (1989) Improved fiber-optic interferometer for atomic force microscopy. *Appl Phys Lett* 55:2588–2590.
34. Morita S, Wiesendanger R, Meyer E, eds. (2002) *Noncontact Atomic Force Microscopy* (Springer, New York).

Supporting Information

Cockins et al. 10.1073/pnas.0912716107

SI Text

Figure Details. The tip height for the voltage spectra and all of the constant height images was 19 ± 1 nm, with the exception of Fig. 5 *D–G* and Fig. S2, where the height was ~23 nm. Additional image details are listed in Table S1. The acquisition time of the majority of spectra was 15 seconds.

Details of Dissipation with Degenerate Shells. Here we outline the approach used to derive the general expression for the dissipation (Eq. **2**). The charging Hamiltonian for small cantilever tip motion may be written

$$H_C = \sum_N E_{C_N}(N - \mathcal{N}_V)^2 |N\rangle\langle N| \simeq H_{C,0} - \sum_N A_N N z |N\rangle\langle N|, \qquad \textbf{[S1]}$$

where $|N\rangle$ is a state with N electrons on the quantum dot (QD), $\mathcal{N}_V = \frac{C_\Sigma(1-\alpha)V_B}{e}$ is the dimensionless gate voltage, C_Σ is the total capacitance of the QD, $H_{C,0}$ is the oscillator-independent part of the charging Hamiltonian, and the coupling strength for given N is $A_N = 2E_{C_N}\partial\mathcal{N}_V/\partial z$. We emphasize that E_C and A may be different for each electron added, as indicated by the index N. From the second equality in Eq. **S1**, N plays the role of a force on the cantilever. As a result, the dissipation and frequency shift may be found from the linear response coefficient $\lambda_N(\omega)$ describing the response of N to changes in z (1).

Consider the charge degeneracy point between N and $N+1$ electrons on the QD, with other charge states prohibited by Coulomb blockade. This may always be viewed as n_{shell} or $n_{shell}+1$ electrons occupying the valence shell of degeneracy ν (even for a nondegenerate single level, for which $n_{shell} = 0$ and $\nu = 1$). Neglecting interactions, the charge state with n_{shell} ($n_{shell}+1$) electrons in the shell is D_n-fold (D_{n+1}-fold) degenerate, with

$$D_n = \binom{\nu}{n_{shell}}, \qquad D_{n+1} = \binom{\nu}{n_{shell}+1}, \qquad \textbf{[S2]}$$

where $\binom{\cdot}{\cdot}$ denotes a binomial coefficient. These arise simply from the different ways to put n_{shell} or $n_{shell}+1$ electrons into ν single particle states. Let $P_{n_{shell},i}$ be the probability to find n_{shell} electrons occupying the shell in configuration i, and $P_{n_{shell}+1,j}$ be the probability to find $n_{shell}+1$ electrons occupying the shell in configuration j. In general, these probabilities will satisfy the master equations (2)

$$\partial_t P_{n_{shell},i} = \sum_j \{\Gamma_{j\to i} P_{n_{shell}+1,j} - \Gamma_{i\to j} P_{n_{shell},i}\}, \qquad \textbf{[S3]}$$

$$\partial_t P_{n_{shell}+1,j} = \sum_i \{\Gamma_{i\to j} P_{n_{shell},i} - \Gamma_{j\to i} P_{n_{shell}+1,j}\}, \qquad \textbf{[S4]}$$

where $\Gamma_{i\to j}$ is the rate to add an electron to configuration i producing configuration j, and vice versa for $\Gamma_{j\to i}$ (note that these rates are nonzero only for configurations i and j that differ by the addition or removal of one electron). We calculate the rates by using Fermi's golden rule.

The master equations (Eqs. **S3** and **S4**) may be solved in general for given values of ν and n_{shell}, but the solutions are cumbersome for highly degenerate shells. To simplify the equations we assume that for a given charge degeneracy point (i.e., a single dissipation peak), the tunneling matrix elements from Fermi's golden rule are equal for all single particle states within the degenerate shell. This is an approximation, because degenerate states may indeed have different wave functions leading to different tunneling rates. However, we expect the rates to be similar because the tunnel barrier between the QD and the two-dimensional electron gas extends over the entire QD area, minimizing the effects of the spatial variations of different wave functions. Moreover, we checked that significantly unequal rates lead only to very small corrections in the peak shifts. For example, taking distinct rates for the two degenerate orbital states in the p shell, we find that rates differing by a factor of 2 lead to a correction of 1.5% for the shift of the 3rd dissipation peak (i.e., the 1st peak in the p shell). We thus neglect these possible differences here. Taking the rates to be equal we arrive at the simplified master equation for the total probability to find n_{shell} electrons in the shell,

$$\partial_t P_{n_{shell}} = \Gamma_-(1 - P_{n_{shell}}) - \Gamma_+ P_{n_{shell}}, \qquad \textbf{[S5]}$$

where

$$\Gamma_+ = (\nu - n_{shell})\Gamma f(E), \qquad \Gamma_- = (n_{shell}+1)\Gamma[1 - f(E)] \qquad \textbf{[S6]}$$

are the rates to add (+) or remove (−) an electron and f is the Fermi function. Note that the master equation for $P_{n_{shell}+1}$ is not independent, because $P_{n_{shell}} + P_{n_{shell}+1} = 1$. The stationary solution of Eq. **S5** is

$$P_{n_{shell}} = \frac{(n_{shell}+1)}{\phi}(1 - f), \qquad \textbf{[S7]}$$

$$P_{n_{shell}+1} = \frac{(\nu - n_{shell})}{\phi} f, \qquad \textbf{[S8]}$$

where ϕ is defined in Eq. **3** of the main text.

The quantity we need is the linear response coefficient $\lambda_N(\omega)$. To find this, we assume that the cantilever is oscillating at frequency ω. This causes the chemical potential difference between the QD and the two-dimensional electron gas to oscillate:

$$E \to E + \delta e^{-i\omega t}, \qquad \textbf{[S9]}$$

and this leads to a change in the probabilities:

$$P_{n_{shell}+1} \to P_{n_{shell}+1} + \lambda_N(\omega)\delta e^{-i\omega t}, \qquad \textbf{[S10]}$$

$$P_{n_{shell}} \to P_{n_{shell}} - \lambda_N(\omega)\delta e^{-i\omega t}. \qquad \textbf{[S11]}$$

Inserting Eqs. **S7–S11** into Eq. **S5** and linearizing in δ, we solve for $\lambda_N(\omega)$. Its real and imaginary part yield the dissipative and conservative parts of the electrostatic force from $(k_0/\omega_0^2)\gamma = -A^2\Im\{\lambda_N(\omega)\}/\omega$ and $(2k_0/\omega_0)\Delta\omega = A^2\Re\{\lambda_N(\omega)\}$. The dissipation for arbitrary degeneracy is given in Eq. **2**, and for the frequency shift we obtain

$$\Delta\omega = -\frac{\omega_0}{2k_0}\frac{A^2\Gamma^2}{k_B T}\left[\frac{(n_{shell}+1)(\nu - n_{shell})}{\omega^2 + (\phi\Gamma)^2}\right] f(1-f). \qquad \textbf{[S12]}$$

Note that we recover the single-level result [i.e., Eq. **1** for the dissipation] by taking $\nu = 1$ and $n_{shell} = 0$ as expected. Finally, we point out that the temperature-dependent level repulsion discussed in the paper is contained in a symmetry of Eq. **2** and

Eq. **S12**, from which we find that taking $n_{\rm shell} \to \nu - n_{\rm shell} - 1$ is equivalent to $E \to -E$.

The peak shifts of γ and $\Delta\omega$ are proportional to temperature and we can solve for the coefficients analytically. However, in general the coefficients are complicated and unenlightening. To show how the peak shifts depend on degeneracy, we provide the coefficients in the low- and high-frequency limits where they are greatly simplified. Note that our experiment is in the intermediate regime $\omega \sim \Gamma$, so the peak shifts measured and calculated in the main text lie between these two limits. For γ, the peak shifts in the low and high frequency limits are

$$\frac{\Delta E_{\gamma,\rm peak}}{k_{\rm B}T} \to \begin{cases} \ln\left(d + \sqrt{d(d+1)+1}\right) & \text{as } (\omega \to 0), \\ \ln\sqrt{d+1} & \text{as } (\omega \to \infty), \end{cases} \quad \textbf{[S13]}$$

where

$$d = \frac{\nu - n_{\rm shell}}{n_{\rm shell}+1} - 1. \quad \textbf{[S14]}$$

For a nondegenerate level, $d = 0$ and there is no peak shift at any frequency. For $\Delta\omega$, the peak shifts in the same two limits are

$$\frac{\Delta E_{\Delta\omega,\rm peak}}{k_{\rm B}T} \to \begin{cases} \ln(d+1) & \text{as } (\omega \to 0), \\ 0 & \text{as } (\omega \to \infty). \end{cases} \quad \textbf{[S15]}$$

Comparing these limits, we see that the shell degeneracy results in a greater peak shift in γ than in $\Delta\omega$. This is a direct consequence of Eq. **4**, from which we see that, aside from an energy-independent prefactor, $\Delta\omega$ differs from γ by a factor of ϕ.

We measured the separation between the peak in γ and the peak in $\Delta\omega$ for each charge degeneracy point. This is shown in Fig. S1 for the third peak in Fig. 2*A* as a function of temperature and compared to theory with no fit parameters. As argued in the main text, this provides strong evidence that the observed peak shifts are indeed a result of shell degeneracy.

Conductance Through a Quantum Dot with Degenerate Shells. It is straightforward to compare our result for the dissipation to the conductance through a QD with degenerate energy levels. The result is essentially contained in ref. 2, but here we provide the extension to arbitrary degeneracy for direct comparison with our Eq. **3**. In a conductance measurement, the QD is placed between two electrodes with an applied drain-source bias voltage $V_{\rm ds}$, and electrons may tunnel on and off the QD via both electrodes. As above, we consider the degeneracy point with $n_{\rm shell}$ or $n_{\rm shell}+1$ electrons in the valence shell, and assume that the tunneling rates to different states within a degenerate shell are equal (for each electrode). For direct comparison with our setup, we further assume that the tunneling rates to the left and right electrodes are equal. In this case, the analog of Eq. **S5** for the conductance is

$$\partial_t P_{n_{\rm shell}} = (\Gamma_{L-} + \Gamma_{R-})(1 - P_{n_{\rm shell}}) - (\Gamma_{L+} + \Gamma_{R+})P_{n_{\rm shell}}, \quad \textbf{[S16]}$$

where $\Gamma_{L(R)+} = (\nu - n_{\rm shell})\Gamma f_{L(R)}$ is the rate to add an electron to the QD from the left (right) lead, and $\Gamma_{L(R)-} = (n_{\rm shell}+1)\Gamma(1 - f_{L(R)})$ is the rate to remove an electron from the QD via the left (right) lead. The Fermi functions in the left and right electrodes are evaluated at the chemical potentials $\mu_L = \mu_0 - eV_{\rm ds}/2$ and $\mu_R = \mu_0 + eV_{\rm ds}/2$, where μ_0 is the chemical potential at $V_{\rm ds} = 0$. We solve Eq. **S16** for the stationary solution of $P_{n_{\rm shell}}$, and calculate the steady state current by considering the electrons tunneling between the QD and, say, the left electrode. Taking the derivative with respect to $V_{\rm ds}$ and taking the $V_{\rm ds} \to 0$ limit yields the zero bias conductance,

$$G = \frac{e^2}{h}\frac{\Gamma}{2k_{\rm B}T}(\nu - n_{\rm shell})(n_{\rm shell}+1)\frac{f(1-f)}{\phi}, \quad \textbf{[S17]}$$

where the argument of the Fermi function is the chemical potential mismatch at zero bias, $E = \mu_{\rm QD} - \mu_0$. We see that the conductance is very similar in form to the dissipation in Eq. **3** but, because there is no cantilever in the conductance setup, it is missing the factor $1/[\omega^2 + (\phi\Gamma)^2]$ (in addition to overall E-independent factors). This factor in the dissipation (and the frequency shift) reflects the interplay of the cantilever and tunneling time scales and depends on E through ϕ. Whereas the effects on the line shape and broadening are small (just as the asymmetric line shape because of degeneracy was too small to be resolved in the dissipation), the effect on the peak shifts is significant. The peak shift in the conductance as a function of d [cf. Eq. **S14**] is

$$\frac{\Delta E_{G,\rm peak}}{k_{\rm B}T} = \ln\sqrt{d+1}. \quad \textbf{[S18]}$$

This is equal to the peak shift in the dissipation in the high frequency limit, but at low frequencies the peak shift in the dissipation is considerably larger. For the frequencies and parameters of our experiment, the peak shifts in the dissipation are roughly a factor of 2 larger than those expected for the conductance.

1. Clerk AA, Bennett S (2005) Quantum nanoelectromechanics with electrons, quasiparticles and cooper pairs: Effective bath descriptions and strong feedback effects. *New J Phys* 7:238.

2. Beenakker CWJ (1991) Theory of Coulomb-blockade oscillations in the conductance of a quantum dot. *Phys Rev B* 44:1646–1656.

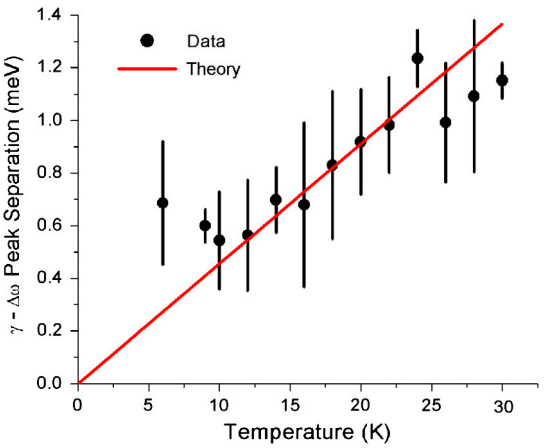

Fig. S1. Difference between dissipation and frequency shift peak positions as a function of temperature for peak 3, compared to theoretical prediction with no fit parameters.

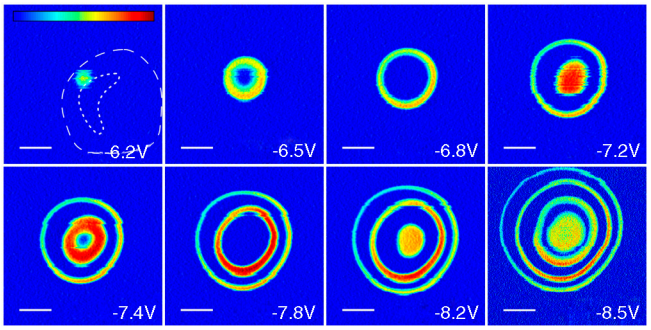

Fig. S2. A series of constant height dissipation images, for the QD shown in Fig. 5 *D–G*, for increasingly negative V_B. The base of the InAs structure is outlined with rectangular dashes and the highest area is outlined with rounded, more closely spaced, dashes. This QD is localized near a high point in the structure, which is often observed. For increasingly negative V_B more rings emerge as the QD is populated with electrons. In these images the ring line shape is broadened by the large cantilever oscillation amplitude of 0.8 nm at 4.5 K with a tip–sample gap of roughly 23 nm. Note that the lateral position of the final image is slightly offset from the others because this image was taken at a later time in the experiment. Notice streaks appear in the same ring location indicating some nearby electrostatic influence. The same color bar was used for each image, with all images but the last having a range of 0–0.85 Hz and the last 0–2 Hz. (Scale bar: 20 nm.)

Table S1. Experimental details of AFM images

Fig.	T (K)	$\Delta\omega/2\pi$ (Hz)	Oscillation amplitude (nm)	V_B (V)	Acquisition time (min.)
1*C*	78	−9.4	1.6	−0.35	6
1*D*	4.5	-	0.4	−8.0	119
1*E*	4.5	-	0.4	−8.0	119
4*A*	4.5	-	0.4	−9.0	17
4*B*	4.5	-	0.4	−7.6	17
4*C*	78	−9.4	1.6	−0.35	14
4 *D–E*	4.5	-	0.4	−8.0	51
5*A*	78	−9.4	1.6	−0.35	9
5*B*	78	-	1.6	−8.0	68
5*C*	4.5	-	0.4	−8.0	51
5*D*	4.5	-	0.8	−8.0	9
5*E*	4.5	-	0.8	−9.0	9
5*F*	4.5	-	0.8	+6.8	9
5*G*	4.5	-	0.8	−8.0	9
S2	4.5	-	0.8	-	17 (last image 9)